Three-Dimensional Electromagnetic Imaging of Dielectric Targets by means of the Multiscaling Inexact-Newton Method

MARCO SALUCCI[1,*], GIACOMO OLIVERI[1,2], NICOLA ANSELMI[1], FEDERICO VIANI[1], ALESSANDRO FEDELI[3], MATTEO PASTORINO[3], AND ANDREA RANDAZZO[3]

[1]*ELEDIA Research Center (ELEDIA@UniTN - University of Trento), Via Sommarive 9, 38123 Trento, Italy*
[2]*ELEDIA Research Center (ELEDIA@L2S - UMR 8506), 3 rue Joliot Curie, 91192, Gif-sur-Yvette, France*
[3]*Department of Electrical, Electronic, Telecommunication Engineering, and Naval Architecture, University of Genova, Via Opera Pia 11 A, 16145 Genova, Italy*
[*]*Corresponding author: marco.salucci@eledia.org*

Compiled April 10, 2017

A novel approach for three-dimensional electromagnetic imaging is presented. This technique is a combination of an iterative multiscaling approach with an inexact-Newton method. The multiscaling procedure allows one to iteratively focus the region of interest on the detected target, whereas the inexact-Newton method provides an efficient regularized solution of the nonlinear electromagnetic inverse scattering problem for each scaling step. The proposed method is validated against numerical data with different configuration settings. A preliminary experimental validation is also reported.

OCIS codes: *(100.3190) Inverse problems; (100.6890) Three-dimensional image processing;(110.3200) Inverse scattering.*

http://dx.doi.org/10.1364/ao.XX.XXXXXX

1. INTRODUCTION

In recent years, the electromagnetic imaging (EI) of dielectric targets has been considered as a potential inspection tool, which can be used in a stand alone way or, better, in a synergic way, with other and more consolidated diagnostic modalities (e.g., X-ray or ultrasounds) [1][2][3][4][5][6][7][8][9][10]. In general, when the frequencies at hand are such that the corresponding wavelengths are comparable with the geometrical dimensions of the targets to be inspected, an inverse scattering (IS) problem has to be solved [1][3][11]. In this case, the imaging system measures samples of the electromagnetic field, which is scattered by the target once it has been illuminated by a proper source. As in radar imaging, the measured samples are the input data for algorithms devoted to extract information on the target under test. In this scenario, most tomographic imaging approaches pursue the goal of providing the whole distributions of the dielectric parameters of the target under test. Of course, simplified information can be sufficient in several applications (e.g., the shape and/or the position of the target can be sufficient in non-destructive testing, where a defect in a known structure could be the target to be retrieved). However, the possibility of directly retrieving the distributions of the dielectric parameters of a target (dielectric permittivity and electric conductivity) is just one of the main features of EI at microwave frequencies and this information can be hardly extracted by using other techniques.

Nevertheless, EI methods suffer from several well known limitations. Firstly, the fully nonlinear IS equations [1] must be solved to inspect strong scatterers. As it is well known, this represents a very ill posed problem with a high numerical complexity [11]. Moreover, the nonlinearity is associated to the problem of the possible presence of false solutions, which introduce constraints on the unknowns that can be reconstructed given a certain measurement configuration [12][13][14]. Although several techniques have been proposed in the past to face this problem in a straightforward way, the computational burden still remains prohibitive if a fine discretization (i.e., a high spatial resolution) is required. In summary, two questions essentially arise in addressing full wave nonlinear IS: how to face the nonlinearity and the ill-posedness of the problem and how to reduce the computational complexity without introducing approximations on the model (i.e., Born or Rytov first order approximations). Considerable progress has been made concerning the first question. In fact, very good nonlinear methods and regularization approaches exist. Concerning the regularization procedure, their main limitation is the need to set some parameters, which are essentially application-dependent. In [15][16][17][18] the present authors have developed an approach based on an

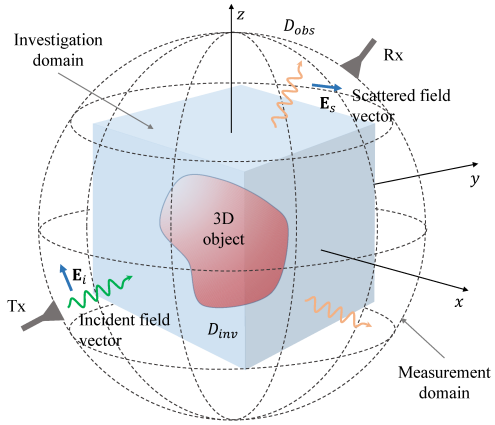

Fig. 1. Three-dimensional imaging configuration: investigation domain D_{inv} and observation domain D_{obs}.

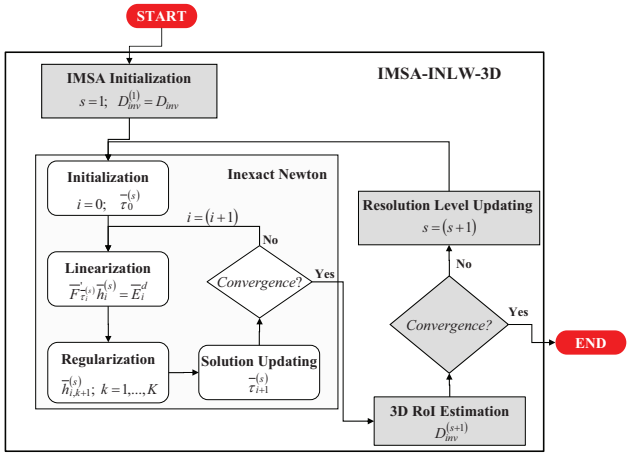

Fig. 2. Flow chart of the IMSA-INLW-3D method.

inexact-Newton/Landweber scheme (INLW) that is composed by two nested loops and provides quite good reconstructions with both synthetic and real input data. As far as the computational complexity is concerned, it has been addressed in several different ways in the scientific literature. Recently, sparsity concepts have been exploited (e.g., in the application of the so called compressive sensing [19][20][21][22]) or hybrid formulations have been applied in which the features of approximate and rigorous IS methods are combined according to suitable strategies for improving the overall solution quality [3]. Another point of view is the iterative focusing of the solution towards the regions of interest (RoIs) in which the target is estimated to lie. In such a way, all the computational resources can be spent to reconstruct the dielectric distributions of such regions, fulfilling the theoretical requirements based on the degrees of freedom of the scattered electromagnetic field [12]. In this framework, preliminary ideas concerning the possibility of such kind of focusing have been initially proposed in [23][24][25][26]. Following these suggestions, an iterative multiscale focusing approach (IMSA) has been introduced in [27] and successively assessed in [28][29]. The idea of combining the INLW method with the IMSA has been proposed in [30] and then extended in [31] for inspecting targets buried in a homogeneous half space. However, these approaches, as most of the ones so far proposed for the solution of IS problems, have been developed with reference to two-dimensional (2D) configurations illuminated by transverse magnetic (TM) and electric (TE) incident waves [32][33][34]. This formulation is valid only for cylindrical targets whose dielectric properties do not change (or change very slowly) along one of the coordinates (corresponding to the cylindrical axis). Conversely, inspecting 3D targets requires to consider the full vector 3D inverse scattering problem, which is more complex than the corresponding 2D scalar one involved in 2D imaging. Although the idea of 3D EI is old [35][36], only today computer power makes it possible to address quite realistic targets. Accordingly, 3D imaging methods have been recently proposed and tested (see, for example, [37][38][39][40][41][42][43][44] and the references therein). However, the computational complexity remains a key issue. In this context, this paper proposes for the first time the application of the combined strategy INLW/IMSA to 3D configurations (IMSA-INLW-3D) starting from input data obtained by the full wave solution of Maxwell equations. The choice of combining 3D IN strategies with multi-scaling solution techniques is motivated by the fact that (*i*) iterative multi-focusing methods keep (at each discretization step) the ratio between the available independent data and the number of unknowns as large as possible [27][28][30], thus reducing the occurrence of local minima [14] in the associated 3D inverse problem, (*ii*) accordingly, effective algorithms based on local search methods operating on iterative linearized formulations of the inverse scattering equations [45] can be effectively used avoiding local minima issues, and (*iii*) IMSA strategies also enable a significant mitigation of computational complexity issues with respect to their "bare" counterparts, which is of fundamental importance when complex 3D scenarios are at hand. Despite such advantages, integrated IMSA-IN techniques have never been developed and validated in 3D formulations, and the associated operative guidelines and achievable performance have not been investigated.

In the following, the mathematical formulation of the approach is described in details in Section 2, whereas Section 3 reports a wide numerical analysis aimed at evaluating capabilities and limitations of the proposed approach. A preliminary experimental result has also been included. Finally, some conclusions are drawn in Section 4.

2. MATHEMATICAL FORMULATION

Let us consider a 3D inhomogeneous scatterer located in a homogeneous background (free space), as sketched in Fig. 1. The target is characterized by a complex dielectric permittivity given by $\tilde{\epsilon}(\mathbf{r}) = \epsilon_0(\epsilon_r(\mathbf{r}) - j\frac{\sigma(\mathbf{r})}{\omega\epsilon_0})$, where ϵ_0 is the vacuum dielectric permittivity, $\epsilon_r(\mathbf{r})$ is the relative permittivity, and $\sigma(\mathbf{r})$ is the electric conductivity, both of them changing with the position vector $\mathbf{r}$. In this paper, we consider a multi-static and multi-view ($v = 1, ..., V$, V being the number of views) measurement configuration. However, in the following mathematical formulation, only a single view ($V = 1$) case is treated, the extension to the multi-view ($V > 1$) configuration being straightforward.

A. Electromagnetic model

The target, which is assumed to be non-magnetic (i.e., with a magnetic permeability $\mu(\mathbf{r}) = \mu_0$, μ_0 being the magnetic permeability of vacuum) is illuminated by an incident electromagnetic field $\mathbf{E}_i(\mathbf{r}) = E_i^x(\mathbf{r})\,\hat{x} + E_i^y(\mathbf{r})\,\hat{y} + E_i^z(\mathbf{r})\,\hat{z}$, $\mathbf{H}_i(\mathbf{r}) =$

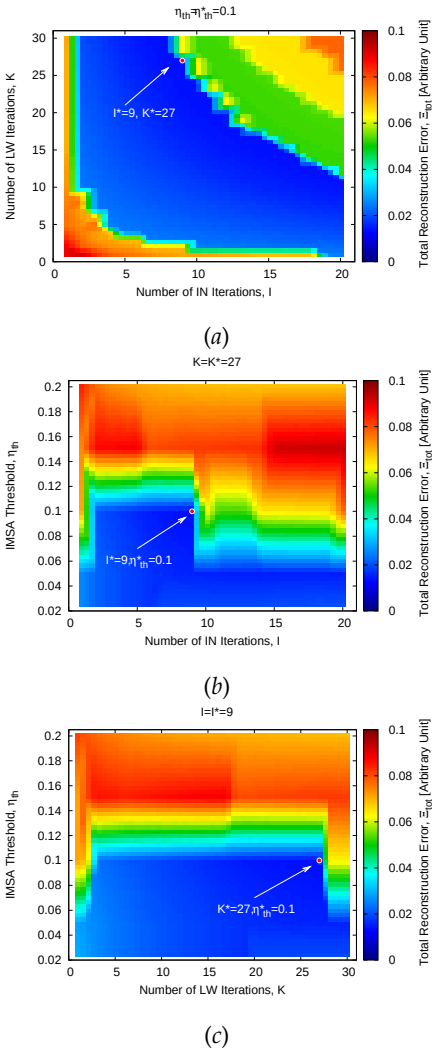

Fig. 3. Calibration with $SNR = 20\,dB$. Total reconstruction error, 2D cuts: (a) number of Landweber iterations vs. number of inexact-Newton iterations; (b) IMSA threshold value vs. number of inexact-Newton iterations; (c) IMSA threshold value vs. number of Landweber iterations.

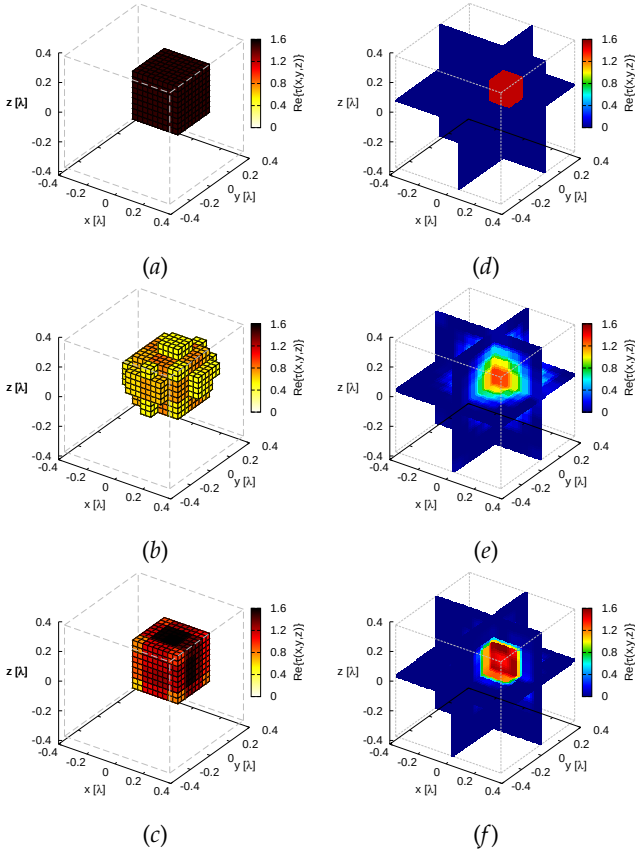

Fig. 4. Comparison between IMSA-INLW-3D and the bare INLW-3D approach. Three-dimensional representations of the contrast function τ in the investigation domain D_{inv}. Voxels having $\Re\{\tau(x,y,z)\} > 0.5$: (a) true object; (b) bare INLW-3D reconstruction; (c) IMSA-INLW-3D reconstruction with $s = s^{best} = 4$. Cuts along the three coordinate planes: (d) true object; (e) bare INLW-3D reconstruction; (f) IMSA-INLW-3D reconstruction with $s = s^{best} = 4$. Dielectric cube used for calibration, $SNR = 20\,dB$.

$H_i^x(\mathbf{r})\,\hat{x} + H_i^y(\mathbf{r})\,\hat{y} + H_i^z(\mathbf{r})\,\hat{z}$. The background medium is vacuum (characterized by ϵ_0 and μ_0). Under these assumptions, the following Maxwell's equations hold:

$$\nabla \times \mathbf{E}(\mathbf{r}) = -j\omega\mu_0 \mathbf{H}(\mathbf{r}) \quad (1)$$

$$\nabla \times \mathbf{H}(\mathbf{r}) = +j\omega\tilde{\epsilon}(\mathbf{r})\,\mathbf{E}(\mathbf{r}) \quad (2)$$

where a time-dependence $e^{j\omega t}$ has been assumed and omitted in the following. By using the equivalence principle and splitting the total field vectors $\mathbf{E}(\mathbf{r}) = E^x(\mathbf{r})\,\hat{x} + E^y(\mathbf{r})\,\hat{y} + E^z(\mathbf{r})\,\hat{z}$, $\mathbf{H}(\mathbf{r}) = H^x(\mathbf{r})\,\hat{x} + H^y(\mathbf{r})\,\hat{y} + H^z(\mathbf{r})\,\hat{z}$ as the sum of the incident and scattered fields (that is, $\mathbf{E}(\mathbf{r}) = \mathbf{E}_i(\mathbf{r}) + \mathbf{E}_s(\mathbf{r})$, $\mathbf{H}(\mathbf{r}) = \mathbf{H}_i(\mathbf{r}) + \mathbf{H}_s(\mathbf{r})$), the equations below can be deduced from (1) and (2) [46]

$$\nabla \times \mathbf{E}_s(\mathbf{r}) = -j\omega\mu_0 \mathbf{H}_s(\mathbf{r}) \quad (3)$$

$$\nabla \times \mathbf{H}_s(\mathbf{r}) = +j\omega\epsilon_0 \mathbf{E}_s(\mathbf{r}) + \epsilon_0\tau(\mathbf{r})\,\mathbf{E}(\mathbf{r}) \quad (4)$$

where τ is the so-called contrast function, which is given by $\tau(\mathbf{r}) = \frac{\tilde{\epsilon}(\mathbf{r})-\epsilon_0}{\epsilon_0} = \epsilon_r(\mathbf{r}) - j\frac{\sigma(\mathbf{r})}{\omega\epsilon_0} - 1$. The resulting scattered field $\mathbf{E}_s(\mathbf{r}) = E_s^x(\mathbf{r})\,\hat{x} + E_s^y(\mathbf{r})\,\hat{y} + E_s^z(\mathbf{r})\,\hat{z} = \mathbf{E}(\mathbf{r}) - \mathbf{E}_i(\mathbf{r})$, i.e., the solution of (3) and (4), can be expressed in integral form as [3]

$$\mathbf{E}_s(\mathbf{r}) = -\omega^2\mu_0\epsilon_0 \int_{D_{inv}} \tau\left(\mathbf{r}'\right)\mathbf{E}\left(\mathbf{r}'\right)\cdot\overline{\mathbf{G}}_0\left(\mathbf{r},\mathbf{r}'\right)d\mathbf{r}' \quad (5)$$

where $\overline{\mathbf{G}}_0$ is the dyadic Green's function for free space [46]. The integral in (5) should be extended to the volume occupied by the target. However, since it is a problem unknown, we assume the object to be included in the fixed volume D_{inv} (i.e., the investigation domain of Fig. 1). If the total field $\mathbf{E}(\mathbf{r})$ is known from measurements outside D_{inv}, (5) turns out to be a nonlinear integral equation describing the full three-dimensional vector inverse problem. The unknowns are represented by τ and the vector field $\mathbf{E}(\mathbf{r})$ inside D_{inv}. Equation (5) can be rewritten in operator form as ("data equation")

$$\mathbf{E}_s(\mathbf{r}) = \Psi_D(\tau\mathbf{E})(\mathbf{r}), \quad \mathbf{r} \notin D_{inv} \quad (6)$$

with

$$\Psi_D\mathbf{f}(\mathbf{r}) = -\omega^2\mu_0\epsilon_0 \int_{D_{inv}} \mathbf{f}(\mathbf{r})\cdot\overline{\mathbf{G}}_0(\mathbf{r},\mathbf{r}')\,d\mathbf{r}', \; \mathbf{r} \notin D_{inv} \quad (7)$$

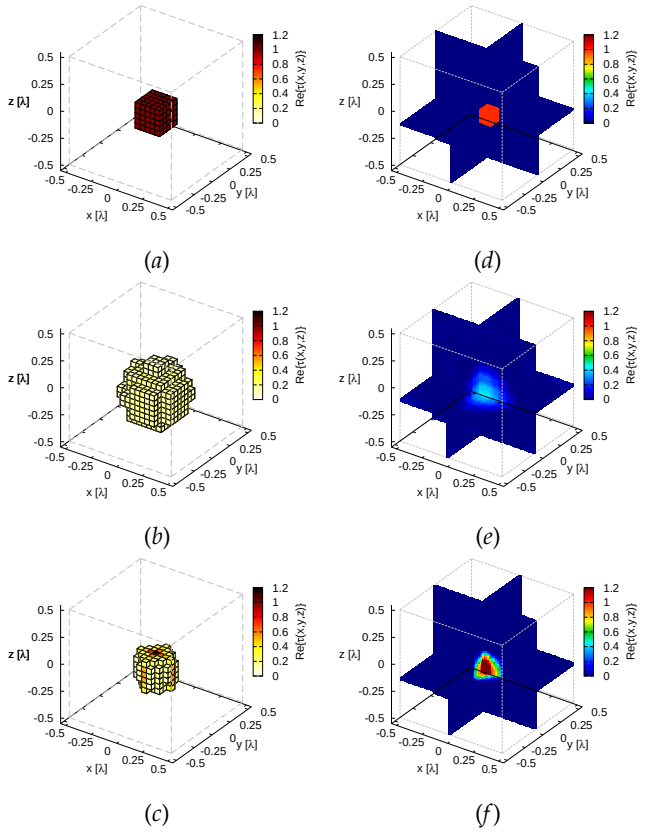

Fig. 5. Three-dimensional representations of the contrast function τ in the investigation domain D_{inv}. Voxels having $\Re\{\tau(x,y,z)\} > 0.1$: (a) true object; (b) bare INLW-3D reconstruction; (c) IMSA-INLW-3D reconstruction with $s = s^{best} = 6$. Cuts along the three coordinate planes: (d) true object; (e) bare INLW-3D reconstruction; (f) IMSA-INLW-3D reconstruction with $s = s^{best} = 6$. Dielectric cube, $SNR = 20\,dB$.

In order to solve (6), a second operator equation is needed. It is obtained by evaluating (5) at points inside D_{inv} ("state equation"), that is,

$$\mathbf{E}_i(\mathbf{r}) = \mathbf{E}(\mathbf{r}) - \mathbf{\Psi}_S(\tau\mathbf{E})(\mathbf{r}), \quad \mathbf{r} \in D_{inv} \tag{8}$$

where the involved operator is defined as

$$\mathbf{\Psi}_S\mathbf{f}(\mathbf{r}) = -\omega^2\mu_0\epsilon_0 \int_{D_{inv}} \mathbf{f}(\mathbf{r}) \cdot \overline{\mathbf{G}}_0(\mathbf{r},\mathbf{r}')\, d\mathbf{r}', \; \mathbf{r} \in D_{inv} \tag{9}$$

Equations (6) and (8) can be combined together in order to obtain the operator vector equation

$$\begin{aligned} \mathbf{E}_s(\mathbf{r}) &= \mathbf{\Psi}_D\left(\mathbf{T}\left(\left(\mathbf{I} - \mathbf{\Psi}_S\mathbf{T}\right)^{-1}\mathbf{E}_i\right)\right)(\mathbf{r}) \\ &= \mathbf{F}(\tau)(\mathbf{r}), \quad \mathbf{r} \notin D_{inv} \end{aligned} \tag{10}$$

where $\mathbf{T}$ is an operator defined as $\mathbf{T}(\mathbf{g})(\mathbf{r}) = \tau(\mathbf{r})\,\mathbf{g}(\mathbf{r})$, $\mathbf{r} \in D_{inv}$. Starting from this equation, the goal of the inverse scattering problem is to retrieve the unknown contrast function τ in the investigation domain D_{inv} given the measured scattered electric field $\mathbf{E}_s$ inside the so-called observation domain D_{obs}. A numerical counterpart of (10) can be obtained after the discretization of the continuous model. In particular, D_{inv} is partitioned into N cubic cells (voxels) and the field vector $\mathbf{E}$ is assumed to be measured in a set of M measurement points located outside D_{inv} and constituting the observation domain D_{obs}. The equation can be written as

$$\bar{E}_s = \bar{F}(\overline{\tau}) \tag{11}$$

where $\bar{E}_s$ is a $3M$-element array containing the values of the three components of the scattered field vector measured at the M measurement points, i.e., $\bar{E}_s = [E_s^x(\mathbf{r}_1), E_s^y(\mathbf{r}_1), E_s^z(\mathbf{r}_1), \ldots, E_s^x(\mathbf{r}_M), E_s^y(\mathbf{r}_M), E_s^z(\mathbf{r}_M)]^T$, and $\overline{\tau} = [\tau(\mathbf{r}_1), \ldots, \tau(\mathbf{r}_N)]^T$ is an array containing the N values of the contrast function at the centers of the N voxels in which D_{inv} is divided. Finally, $\bar{F}$ denotes the discretized counterpart of the operator $\mathbf{F}$. In order to acquire multi-illumination multi-view information, the target is successively illuminated by a set of V incident field vectors $\mathbf{E}_i^v$, $v = 1, \ldots, V$. In this case, the size of the numerical array containing the scattered field data is multiplied by a factor V.

B. Multiscaling inversion algorithm

The inversion of the nonlinear scattering equation (11) to reconstruct the contrast function τ gives rise to a strongly ill-posed problem. Therefore, we adopt here the INLW method presented in [15][17][18] combined with the IMSA strategy [27][28][30]. A flow chart of the developed integrated inversion strategy is shown in Fig. 2.

In general, for each IMSA focusing step, the domain is discretized according to a (non-uniform) 3D grid in which the dimension of each voxel is iteratively adapted to reduce their volume in the detected scatterer region, while keeping the overall number of voxels (i.e., unknowns) as close as possible to the amount of available information [27][28][30]. It is worth noting that this is not in general sufficient to completely avoid local minima [14]. However, IMSA tries to keep the ratio between independent data and unknowns as large as possible to increase the robustness with respect to false solutions. Such a procedure is particularly challenging in the 3D case since (*i*) at each iteration, the multi-scale gridding of the investigation domain must guarantee the coherence of the final voxel layout (i.e., the entire volume under investigation must be fully discretized), which is much more complex to be met than in the 2D case, and (*ii*) unlike standard meshing procedures, this goal must be achieved without increasing the total number of voxels in the investigation domain. The s-th step discretized inverse problem is then handled by a Gauss-Newton loop that provides a linearization of the 3D vector scattering equation (10), which is subsequently solved (in a regularized way) with a truncated Landweber technique. More in detail, this combined approach has the following scheme, in which s denotes the IMSA iteration, $D_{inv}^{(s)}$ is the investigation area at the s-th IMSA iteration, and $\overline{\tau}_i^{(s)}$ denotes the array containing the values of the contrast function at the i-th iteration of the solving Gauss-Newton loop at the s-th IMSA iteration.

1. Initialization of the inversion algorithm at the coarsest scale ($s = 1$). In this first step, the investigation domain is discretized using a uniform grid with $N = N_{IMSA}$ voxels (i.e., a relatively "coarse" discretization is used to image the domain), and the associated problem is solved for computing the starting point for the multi-focusing procedure by using the algorithm described in Section C. In this initialization phase, we assume $D_{inv}^{(1)} = D_{inv}$, i.e., the region of interest coincides with the whole investigation area and

Table 1. Relative reconstruction errors for both the bare INLW-3D and the IMSA-INLW-3D approaches. Dielectric cube, $SNR = 20\,dB$.

	INLW-3D	IMSA-INLW-3D
Ξ_{tot}	9.29×10^{-2}	1.38×10^{-2}
Ξ_{int}	2.47×10^{-1}	9.65×10^{-2}
Ξ_{ext}	7.72×10^{-2}	5.57×10^{-3}

it is discretized into N_{IMSA} subdomains. An empty investigation area (i.e., $\overline{\tau}_0^{(1)}$ is a null N -element array) is assumed as initial guess if no information on the target properties is available;

2. At step s, the contrast function $\overline{\tau}^{(s)}$ is found by solving (10) in a regularized sense in the current region of interest $D_{inv}^{(s)}$. To this end, the inexact-Newton approach described in Section C is used.

3. Identification of the new region of interest $D_{inv}^{(s+1)}$ on the basis of the detected target location (e.g., a clustering technique [27] can be used) and discretization of $D_{inv}^{(s+1)}$ into N_{IMSA} cells. More specifically, the barycenter of $D_{inv}^{(s+1)}$ is computed as follows [29]

$$c^{(s+1)} = \frac{\sum_{r=1}^{R(s)} \sum_{n(r)=1}^{N_r^{(s)}} \left\{ c_{n(r)} \tau^{(s)} \left(\mathbf{r}_{n(r)} \right) \right\}}{\sum_{r=1}^{R(s)} \sum_{n(r)=1}^{N_r^{(s)}} \left\{ \tau^{(s)} \left(\mathbf{r}_{n(r)} \right) \right\}} \tag{12}$$

where $c = \{x, y, z\}$ and $R(s) = s$ is the number of resolution levels at the s-th step. Moreover, the side of $D_{inv}^{(s+1)}$ is computed as follows

$$L^{(s+1)} = 2 \frac{\sum_{r=1}^{R(s)} \sum_{n(r)=1}^{N_r^{(s)}} \left\{ \frac{\rho_{n(r)c(s)} \tau^{(s)} \left(\mathbf{r}_{n(r)} \right)}{\max_{n(r)=1,\ldots,N_r^{(s)}} \left\{ \tau^{(s)} \left(\mathbf{r}_{n(r)} \right) \right\}} \right\}}{\sum_{r=1}^{R(s)} \sum_{n(r)=1}^{N_r^{(s)}} \left\{ \frac{\tau^{(s)} \left(\mathbf{r}_{n(r)} \right)}{\max_{n(r)=1,\ldots,N_r^{(s)}} \left\{ \tau^{(s)} \left(\mathbf{r}_{n(r)} \right) \right\}} \right\}} \tag{13}$$

where

$$\rho_{n(r)c(s)} = \sqrt{\left(x_{n(r)} - x^{(s)} \right)^2 + \left(y_{n(r)} - y^{(s)} \right)^2 + \left(z_{n(r)} - z^{(s)} \right)^2}. \tag{14}$$

4. Iteration from step 2 until a predefined number of IMSA scaling steps is reached ($s = S$) or a stationarity criterion is fulfilled, such as

$$\frac{|L^{(s+1)} - L^{(s)}|}{L^{(s)}} < \eta_{th} \tag{15}$$

where η_{th} is a given threshold value. The scaling step s for which the condition (15) is satisfied is denoted as s^{best}.

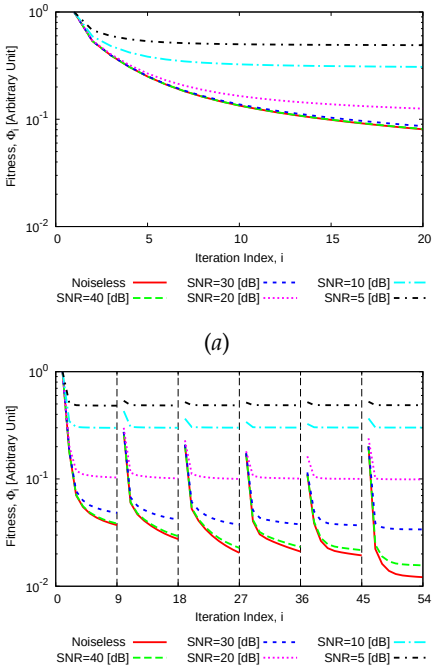

Fig. 6. Evolution of the fitness function Φ versus the iteration number for (a) bare INLW-3D method; (b) IMSA-INLW-3D method for different values of SNR. In the IMSA-INLW-3D method, vertical dashed lines delimit the IMSA steps. Dielectric cube.

C. Inexact-Newton method

According to the algorithm described in Section B, at any IMSA iteration s , the array containing the values of the contrast function is obtained by the following steps [16, 17]:

1. Initialization of the procedure by setting $i = 0$ (i being the iteration index of the outer inexact-Newton loop), with initial guess $\overline{\tau}_0^{(s)}$. In the case of $s > 1$, the reconstruction obtained at the previous scale $s - 1$ is employed for initializing the inexact-Newton method;

2. Linearization of the scattering equation (11) for yielding the linear equation

$$\bar{F}'_{\overline{\tau}_i^{(s)}} \bar{h}_i^{(s)} = \bar{E}_i^d \tag{16}$$

where $\bar{F}'_{\overline{\tau}_i^{(s)}}$ is the Jacobian matrix of $\bar{F}$ calculated at $\overline{\tau}_i^{(s)}$ [45], $\bar{h}_i^{(s)}$ (to be found in the inner loop) is the increment with respect to the currently reconstructed contrast function $\overline{\tau}_i^{(s)}$, and $\bar{E}_i^d = \bar{E}_s - \bar{F}(\overline{\tau}_i^{(s)})$;

3. Computation of a regularized solution of the linear equation (16) with respect to the unknown $\bar{h}_i^{(s)}$, by using a truncated Landweber scheme, i.e.,

$$\begin{cases} \bar{h}_{i,0}^{(s)} = \bar{0} \\ \bar{h}_{i,k+1}^{(s)} = \bar{h}_{i,k}^{(s)} + \\ \quad -\alpha \bar{F}'^{*}_{\overline{\tau}_i^{(s)}} \left(\bar{F}'_{\overline{\tau}_i^{(s)}} \bar{h}_{i,k}^{(s)} - \bar{E}_i^d \right) \end{cases} \tag{17}$$

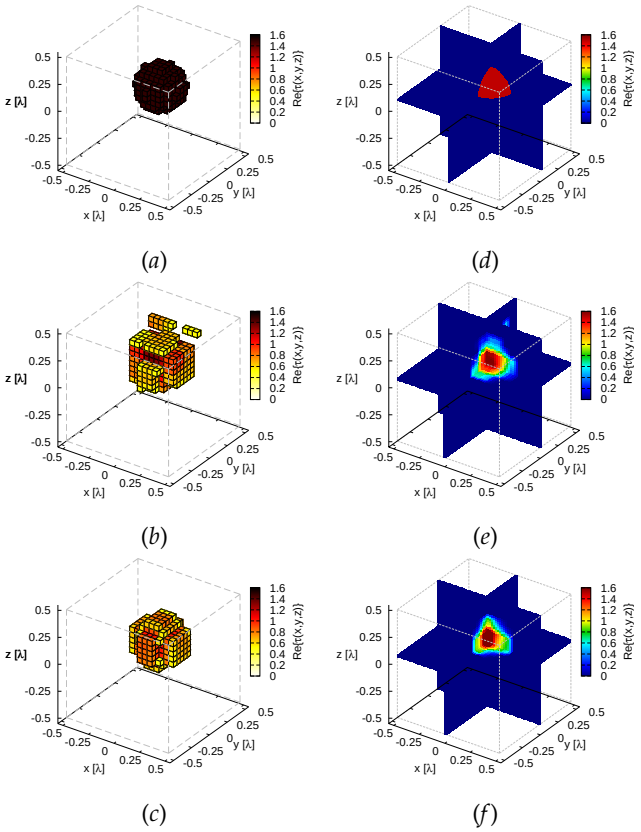

Fig. 7. Three-dimensional representations of the contrast function τ in the investigation domain D_{inv}. Voxels having $\Re\{\tau(x,y,z)\} > 0.5$: (a) true object; (b) IMSA-INLW-3D reconstruction with $SNR = 5\,dB$; (c) IMSA-INLW-3D reconstruction with $SNR = 40\,dB$. Cuts along the three coordinate planes: (d) true object; (e) IMSA-INLW-3D reconstruction with $SNR = 5\,dB$; (f) IMSA-INLW-3D reconstruction with $SNR = 40\,dB$. Dielectric sphere.

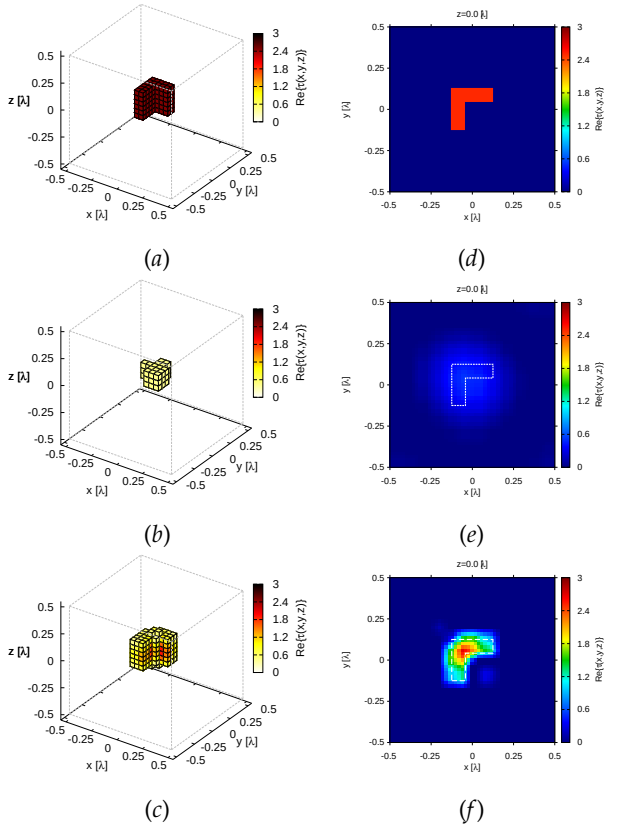

Fig. 8. Three-dimensional representations of the contrast function τ in the investigation domain D_{inv}. Voxels having $\Re\{\tau(x,y,z)\} > 0.5$: (a) true object; (b) bare INLW-3D reconstruction; (c) IMSA-INLW-3D reconstruction with $s = s^{best} = 6$. Two-dimensional cuts for $z = 0$ of the reconstructed distributions of the contrast function τ: (d) true object; (e) bare INLW-3D reconstruction; (f) IMSA-INLW-3D reconstruction with $s = s^{best} = 6$. L-shaped object, $SNR = 20\,dB$.

with $\alpha = \left\| \bar{F}'^{*}_{\bar{\tau}_i^{(s)}} \bar{F}'_{\bar{\tau}_i^{(s)}} \right\|^{-1}$ as constant step length. In (17), $\bar{F}'^{*}_{\bar{\tau}_i^{(s)}}$ denotes the adjoint matrix of $\bar{F}'_{\bar{\tau}_i^{(s)}}$, and k is the inner iteration index. The iterations are stopped when a maximum number of inner steps K is reached;

4. Update of the current contrast function as

$$\bar{\tau}_{i+1}^{(s)} = \bar{\tau}_i^{(s)} + \bar{h}_{i,K}^{(s)}; \tag{18}$$

5. Iteration of the inversion procedure from step 2, setting $i = i+1$, until a predefined stopping criterion is verified or a maximum number of outer Gauss-Newton iterations I is reached;

It is worth noting that the number of inner steps K represents a regularization parameter for the solution of (16) in the nested truncated Landweber algorithm [11]. Therefore, if a proper number of Landweber iterations is executed, a regularizing behavior can be easily obtained.

3. NUMERICAL AND EXPERIMENTAL RESULTS

The IMSA-INLW-3D algorithm has been validated with several numerical simulations. Moreover, a preliminary experimental test has also been performed. The performance of the proposed method has been also compared with the "bare" inexact-Newton approach (INLW-3D), namely the standard inexact-Newton/Landweber inversion method without the IMSA scaling steps. In all simulations, the forward electromagnetic problem has been solved with the method of moments [47]. In order to analyze the impact of the noise, the simulated scattered field data at the measurement points $\mathbf{r} \in D_{obs}$ have been corrupted by adding a Gaussian noise having zero mean value and standard deviation proportional to the signal-to-noise ratio (SNR).

The reconstruction error has been evaluated as

$$\Xi_{reg} = \frac{1}{N_{reg}} \sum_{\mathbf{r}_n \in R_{reg}} \frac{|\tilde{\epsilon}(\mathbf{r}_n) - \tilde{\epsilon}^{*}(\mathbf{r}_n)|}{|\tilde{\epsilon}(\mathbf{r}_n)|} \tag{19}$$

where D_{reg}, with $reg = \{tot, int, ext\}$ indicates the considered region for the error computation, i.e., the whole investigation domain, the actual object support, and the background region,

Table 2. Relative reconstruction errors for both the bare INLW-3D and the IMSA-INLW-3D method, for different values of SNR. Dielectric sphere.

INLW-3D			
$SNR\ (dB)$	Ξ_{tot}	Ξ_{int}	Ξ_{ext}
∞	4.74×10^{-2}	3.02×10^{-1}	3.73×10^{-2}
40	4.74×10^{-2}	3.02×10^{-1}	3.74×10^{-2}
30	4.74×10^{-2}	3.02×10^{-1}	3.74×10^{-2}
20	4.76×10^{-2}	3.02×10^{-1}	3.75×10^{-2}
10	4.83×10^{-2}	3.05×10^{-1}	3.72×10^{-2}
5	5.06×10^{-2}	3.00×10^{-1}	3.83×10^{-2}
IMSA-INLW-3D			
$SNR\ (dB)$	Ξ_{tot}	Ξ_{int}	Ξ_{ext}
∞	1.74×10^{-2}	2.10×10^{-1}	1.07×10^{-2}
40	1.74×10^{-2}	2.10×10^{-1}	1.07×10^{-2}
30	1.74×10^{-2}	2.10×10^{-1}	1.07×10^{-2}
20	1.78×10^{-2}	2.09×10^{-1}	1.07×10^{-2}
10	1.84×10^{-2}	1.83×10^{-1}	1.12×10^{-2}
5	2.91×10^{-2}	1.69×10^{-1}	2.07×10^{-2}

Table 3. Relative reconstruction errors for both the bare INLW-3D and the IMSA-INLW-3D method, for different values of SNR. L-shaped object.

INLW-3D			
$SNR\ (dB)$	Ξ_{tot}	Ξ_{int}	Ξ_{ext}
∞	2.87×10^{-2}	6.10×10^{-1}	2.26×10^{-2}
40	2.87×10^{-2}	6.10×10^{-1}	2.26×10^{-2}
30	2.87×10^{-2}	6.10×10^{-1}	2.26×10^{-2}
20	2.88×10^{-2}	6.10×10^{-1}	2.26×10^{-2}
10	2.91×10^{-2}	6.10×10^{-1}	2.27×10^{-2}
5	2.98×10^{-2}	6.10×10^{-1}	2.29×10^{-2}
IMSA-INLW-3D			
$SNR\ (dB)$	Ξ_{tot}	Ξ_{int}	Ξ_{ext}
∞	9.14×10^{-3}	3.70×10^{-1}	5.85×10^{-3}
40	9.03×10^{-3}	3.69×10^{-1}	5.75×10^{-3}
30	9.12×10^{-3}	3.71×10^{-1}	5.81×10^{-3}
20	9.18×10^{-3}	3.71×10^{-1}	5.77×10^{-3}
10	9.87×10^{-3}	3.88×10^{-1}	5.86×10^{-3}
5	1.36×10^{-2}	3.38×10^{-1}	9.65×10^{-3}

respectively. In (19), $\tilde{\epsilon}(\mathbf{r}_n)$ and $\tilde{\epsilon^*}(\mathbf{r}_n)$ are the actual and the reconstructed values of the dielectric permittivity in the n-th sub-domain, while N_{reg} is the number of cells of the considered region. The fitness function, which quantifies the distance between the reconstructed and the measured scattered electric field, is defined as

$$\Phi = \sqrt{\frac{\sum_{v=1}^{V} \left\| \bar{E}_s^v - \tilde{\bar{E}}_s^v \right\|^2}{\sum_{v=1}^{V} \left\| \bar{E}_s^v \right\|^2}} \tag{20}$$

where $\bar{E}_s^v$ is the array containing all the scattered field measurements (x, y, and z components) at the vth view, and $\tilde{\bar{E}}_s^v$ is the corresponding reconstructed counterpart.

The number of views, the number of measurement points, and the discretization used for solving the IS problem have been chosen on the basis of the degrees of freedom of the scattered field calculated by using the Effective Bandwidth (EB) approach [12][13]. Accordingly, V and M have been set to $V = M = \left\lfloor 12\pi \left(\frac{L_{D_{inv}}}{\lambda}\right)^2 \right\rfloor$, $L_{D_{inv}}$ being the side of a cubic investigation domain, while

$$N_{IMSA} = \left\lfloor \sqrt[3]{72\pi^2 \left(\frac{L_{D_{inv}}}{\lambda}\right)^4} \right\rfloor^3 \tag{21}$$

has been chosen for discretizing the investigation domain D_{inv} in the IMSA-INLW-3D method. The number of cells for discretizing the inversion domain of the "bare" inexact-Newton approach N_{BARE} has been selected to have a resolution smaller or equal to $\lambda/10$ in D_{inv}.

A. Calibration

The most important control parameters of the IMSA-INLW-3D are the number of Gauss-Newton iterations, I, the number of Landweber steps, K, and the IMSA threshold, η_{th}, for the volume-based stopping criterion (15). Because of their impact on the inversion performance, a calibration phase concerned with a benchmark scenario including noisy data has been carried out. To this end, it is worth remarking that the objective of the calibration phase is not that of providing an optimal parameter setup for each possible imaging configuration, but rather to deduce an effective tradeoff guideline for the IMSA-INLW-3D configuration which can be reliably adopted in different scenarios and configurations (as it will be demonstrated in the subsequent numerical validation). Towards this purpose, noisy conditions have been considered ($SNR = 20\,dB$) and a benchmark cubic investigation domain centered at the origin of side $L_{D_{inv}} = 0.75\lambda$ has been assumed. The target under test has been illuminated by plane waves impinging from $V_\theta = 6$ directions on θ and $V_\phi = 5$ directions on ϕ for a total number of views equal to $V = (V_\theta - 2) \times V_\phi + 2 = 22$. As for the observation domain, it was composed by a set of points located on a sphere of radius $r_{D_{obs}} = \lambda$. In particular, $M_\theta = 6$ and $M_\phi = 5$ field measurements have been taken on θ and ϕ, respectively, with a total number of $M = (M_\theta - 2) \times M_\phi + 2 = 22$ measurements. The actual scatterer was a cube with side length $l_{obj} = 0.3\lambda$ centered at $\left(x_{obj}, y_{obj}, z_{obj}\right) = (0.075, 0.075, 0.075)\,\lambda$ and characterized by a contrast function $\tau = 1.5$. The forward problem has been solved discretizing the investigation domain into $N_{fwd} = 9261$ cubic cells of side $l_{fwd} = 0.036\lambda$, while $N_{IMSA} = 216$ cells have been used for the inversion

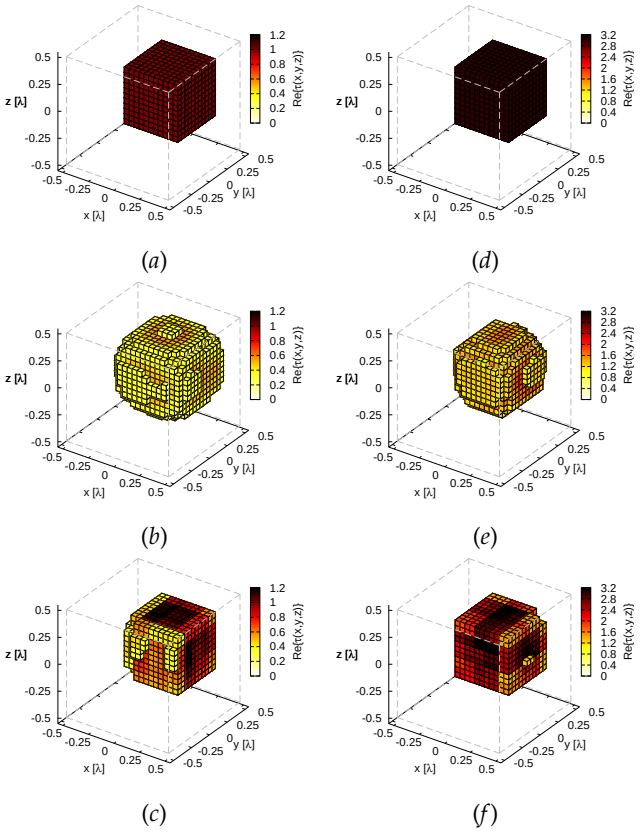

Fig. 9. Three-dimensional representations of the contrast function τ in the investigation domain D_{inv} for $SNR = 20\,dB$, with different methods and object contrast functions. Voxels having $\Re\{\tau(x,y,z)\} > 0.5$: (a) actual profile, $\tau = 1.0$; (b) INLW-3D, $\tau = 1.0$; (c) IMSA-INLW-3D, $\tau = 1.0$; (d) actual profile, $\tau = 3.0$; (e) INLW-3D, $\tau = 3.0$; (f) IMSA-INLW-3D, $\tau = 3.0$. Cube object.

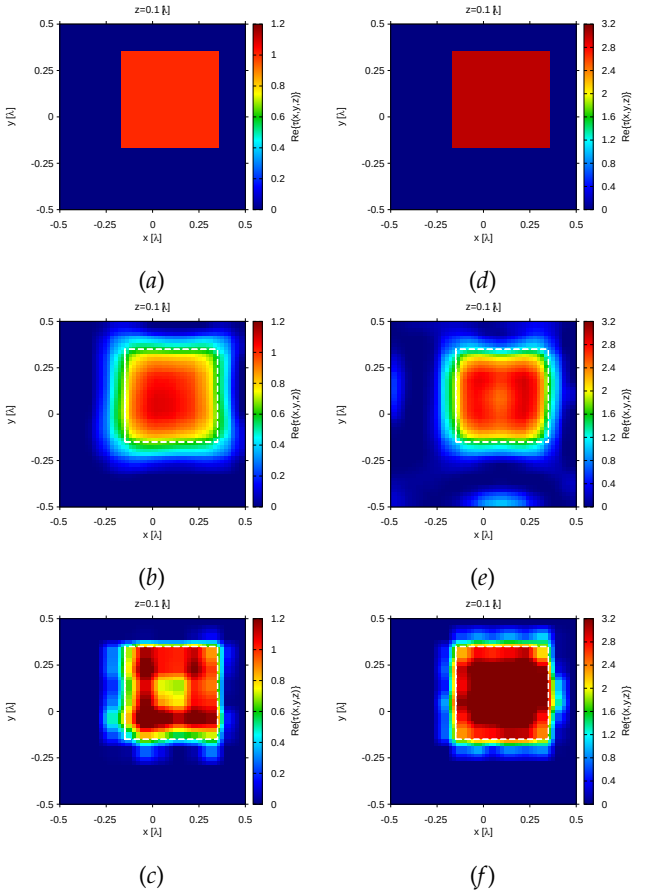

Fig. 10. Two-dimensional cuts for $z = 0$ of the actual and reconstructed distributions of the contrast function τ of the investigation domain D_{inv} for $SNR = 20\,dB$, with different methods and object contrast functions: (a) actual profile, $\tau = 1.0$; (b) INLW-3D, $\tau = 1.0$; (c) IMSA-INLW-3D, $\tau = 1.0$; (d) actual profile, $\tau = 3.0$; (e) INLW-3D, $\tau = 3.0$; (f) IMSA-INLW-3D, $\tau = 3.0$. Cube object.

method. The control parameters have been varied within the following ranges: $I = \{1,2,\ldots,20\}$, $K = \{1,2,\ldots,30\}$, and $\eta_{th} = \{0.025, 0.05, 0.1, 0.15, 0.2\}$. A maximum number of IMSA scaling steps $S = 6$ has been fixed. The total reconstructions errors (19) versus the three calibration parameters are reported in Fig. 3. The best reconstruction has been obtained with the setup $I^* = 9$, $K^* = 27$, and $\eta^*_{th} = 0.1$ (where the asterisk indicates the optimal parameters found in calibration), then used as reference in the following.

B. Comparison with the bare inexact-Newton approach

Clearly, a comparison with the "bare" inexact-Newton approach is essential. To this aim, let us consider the same configuration used for the calibration, that is, a middle-sized dielectric cube. All the configuration details and parameters are reported in the "Calibration" Section, the IMSA-INLW-3D control parameters being chosen as in the same Section. The bare INLW-3D method has been applied to the same investigation domain D_{inv}, but discretized into $N_{BARE} = 1000$ cubic cells of side $l_{BARE} = 0.075\lambda$, with $I_{BARE} = 20$ maximum outer Gauss-Newton iterations and $K_{BARE} = 2$ maximum inner Landweber steps [45]. The results of the reconstruction with these different methods versus the true dielectric configuration of the investigation domain are presented in Fig. 4. In this case, the threshold value η^*_{th} determined an optimal number of IMSA steps equal to $s^{best} = 4$. The quality improvement from the use of the IMSA scaling steps into the standard INLW-3D method is evident. With the IMSA-INLW-3D approach [Fig. 4 (c)], the cubic target is better localized, and both the shape and the contrast function τ are closer to the actual ones. Such an enhancement is confirmed by the relative reconstruction errors reported in Table 1.

C. Performance versus the signal-to-noise ratio

In this Section, the performance of the proposed IMSA-INLW-3D method versus the SNR is analyzed. Several targets with different shapes and dimensions have been considered in various operating conditions with $SNR = \{5, 10, 20, 30, 40, \infty\}\ dB$. In all cases, a cubic investigation domain D_{inv} of side $L_{D_{inv}} = \lambda$, centered at the origin, has been considered. Plane waves originated from $V_\theta = 8$ directions on θ and $V_\phi = 6$ directions on ϕ have been used for illuminating the investigation domain, obtaining a total number of views equal to $V = 38$. The observation domain D_{obs} was composed by $M = 38$ measurement points ($M_\theta = 8$ and $M_\phi = 6$) positioned

on a sphere of radius $r_{D_{obs}} = 2\lambda$. D_{inv} has been partitioned into $N_{fwd} = 9261$ cubic cells of side $l_{fwd} = 0.048\lambda$ for solving the forward problem. The number of subdomains for the IMSA-INLW-3D method has been chosen equal to $N_{IMSA} = 512$, while $N_{BARE} = 1728$ cubic cells of side $l_{BARE} = 0.083\lambda$ have been used for the bare INLW-3D approach.

C.1. Cube object

For a dielectric cube of side $l_{obj} = 0.25\lambda$ with contrast function $\tau = 1.0$, centered at $\left(x_{obj}, y_{obj}, z_{obj}\right) = (0, 0, -0.125)\,\lambda$, the reconstructed contrast distributions when $SNR = 20\,dB$ are shown in Fig. 5 versus the true dielectric configuration. As it can be observed, there is a non-negligible improvement. By analyzing the behavior of the fitness function (20) for different SNRs (Fig. 6), it turns out that the IMSA-INLW-3D approach enables a better modeling of the electric field in the observation domain D_{obs}. This is due to the iterative execution of multiple inexact-Newton procedures, each one performed at a different IMSA scaling step (delimited by vertical dashed lines in the graph). Of course, the lowest fitness function values (i.e., the best reconstructions of the electric field around the object) in both the bare INLW-3D and the IMSA-INLW-3D method are found for the noiseless case. In general, as the SNR decreases, there is an increase in the values of the fitness function Φ. In the IMSA-INLW-3D technique, significant improvements in terms of the fitness function minimization between IMSA steps could be noticed in particular for $SNR > 20\,dB$. Moreover, the IMSA-INLW-3D method is computationally more efficient than the bare INLW-3D approach. In particular, the reduced number of discretization cells in the investigation domain allows to save both computational time and computer memory. For instance, on an Intel(R) Core(TM) i5-2400 CPU at 3.10 GHz personal computer with 4 GB of random access memory, the average computational time per outer inexact-Newton iteration in this case is equal to 3.22×10^2s using the IMSA-INLW-3D method and 1.08×10^3s in the bare INLW-3D algorithm, while the required memory is 263 MB vs. 776 MB, respectively. As a matter of fact, a significant time saving is achieved by the IMSA-INLW-3D to retrieve the electromagnetic properties of D_{inv} (i.e., $\frac{\Delta t|_{IMSA-INLW-3D}}{\Delta t|_{INLW-3D}} \approx 0.42$). Moreover, it is worth pointing out that the additional computational time required at each multiscaling step ($s = 1, ..., s^{best} - 1$) for identifying the RoI ($D_{inv}^{(s+1)}$), updating its barycentre and side through (12) and (13), as well as discretizing it (Fig. 2) is lower than 1 s using a non-optimized code.

C.2. Sphere object

The reconstruction of a spherical dielectric target is now analyzed. The sphere was centered at $\left(x_{obj}, y_{obj}, z_{obj}\right) = (0, 0.1, 0.1)\,\lambda$ with a radius $r_{obj} = 0.2\lambda$ and characterized by a contrast function $\tau = 1.5$. Some IMSA-INLW-3D reconstructions for different SNR values are shown in Fig. 7. Clearly, the lowest SNR value [Fig. 7(*b*) vs. Fig. 7(*c*)] provides a poorer reconstruction. Nevertheless, the dielectric sphere is correctly localized and its retrieved contrast function is near the actual value in both cases. The relative reconstruction errors versus the SNR are given in Tab. 2. Although the IMSA-INLW-3D method seems to be slightly more sensitive to SNR variations, it always provides significantly lower reconstruction errors.

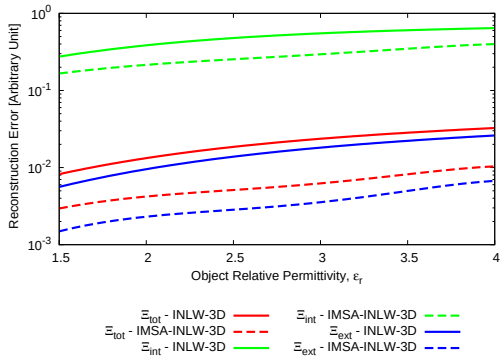

Fig. 11. Relative errors on the reconstruction of the L-shaped object with $SNR = 20\,dB$ versus the object relative dielectric permittivity.

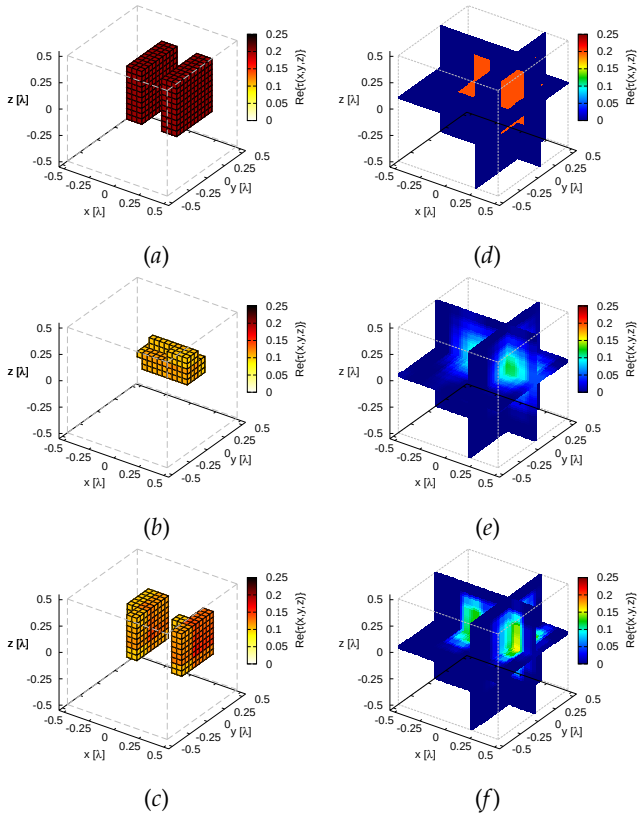

Fig. 12. Three-dimensional representations of the contrast function τ in the investigation domain D_{inv}. Voxels having $\Re\{\tau(x, y, z)\} > 0.1$: (a) true object; (b) bare INLW-3D reconstruction; (c) IMSA-INLW-3D reconstruction with $s = s^{best} = 2$. Cuts along the three coordinate planes: (d) true object; (e) bare INLW-3D reconstruction; (f) IMSA-INLW-3D reconstruction with $s = s^{best} = 2$. Low-contrast target, $SNR = 20\,dB$.

C.3. L-shaped object

The behavior of the inversion method with a more complex target shape is studied in the present Section, in particular with reference to an "L-shaped" dielectric object (Fig. 8*a*). The maximum length of its side is $l_{obj} = 0.25\lambda$ and its contrast function is equal to $\tau = 2.5$. The parameters of both the forward and inverse solution methods are those described in Section "Performance versus the signal-to-noise ratio". In Fig. 8, the 3D representations and the corresponding 2D cuts for $z = 0$ of the reconstructed contrast function in the investigation domain versus the true dielectric configuration are shown when $SNR = 20\,dB$. In particular, the result yielded with the bare INLW-3D method is reported in Fig. 8(*b*) and in Fig. 8(*e*), while in Fig. 8(*c*) and Fig. 8(*f*) there is the IMSA-INLW-3D reconstruction. Once again, the multi-resolution implementation outperforms the bare one by producing a high quality map of the contrast function τ. An analysis of the methods performance versus the data noise level is summarized in Table 3. As it can be noticed, the IMSA-INLW-3D produces the lowest restoration errors.

D. Performance versus the object permittivity

Another key-analysis in assessing the proposed IMSA-INLW-3D method is on the dependence of the inversion accuracy on the object permittivity. In this Section, such a task is accomplished taking into account representative examples dealing with different targets and measurement setups.

D.1. Cube object

With reference to a centered cubic D_{inv} of side $L_{D_{inv}} = \lambda$ illuminated by plane waves impinging from $V_\theta = 3$ and $V_\phi = 4$ directions ($V = 6$) and partitioned into $N_{fwd} = 9261$ cubic cells of side $l_{fwd} = 0.048\lambda$, a measurement setup composed by $M = 82$ measurement points distributed in $M_\theta = 10$ directions on θ and $M_\phi = 10$ directions on ϕ, and positioned on a sphere with radius $r_{D_{obs}} = \lambda$, the IMSA-INLW-3D has been applied by considering $N_{IMSA} = 512$ subdomains with control parameters as in the previous section, while the bare INLW-3D method has been used with $N_{BARE} = 8000$ cells of side $l_{BARE} = 0.05\lambda$, $I_{BARE} = 20$ and $K_{BARE} = 3$ being the control parameter setup [45]. The investigation domain D_{inv} has been assumed to contain a cubic dielectric target with side length $l_{obj} = 0.5\lambda$ and located at $\left(x_{obj}, y_{obj}, z_{obj}\right) = (0.1, 0.1, 0.1)\,\lambda$. The object contrast function τ has been varied in the range $\tau \in [0.5, 3.0]$ with steps of 0.5. Some 3D reconstructions and the corresponding 2D cuts of the retrieved dielectric profile distributions for $SNR = 20\,dB$ are reported in Fig. 9 and Fig. 10. It is worth noting that the performance of this technique versus the bare INLW-3D one seems to improve even more with an increase in the object permittivity. Thanks to the scaling steps, the reconstruction of the actual shape of the scatterer appears to be significantly more faithful.

D.2. L-shaped object

Another set of simulations is concerned with the L-shaped object shown in Fig. 8(*a*). By keeping the same measurement and control parameters setups, the contrast function τ of the actual L-shaped object has been varied between 0.5 and 3.0 with steps of 0.5. Figure 11 plots the relative reconstruction errors referred to the different investigation domain regions versus the target permittivity. As it can be observed, the relative reconstruction error always increases with the object permittivity. However, the errors from the IMSA-INLW-3D method are significantly lower than those with the bare INLW-3D technique.

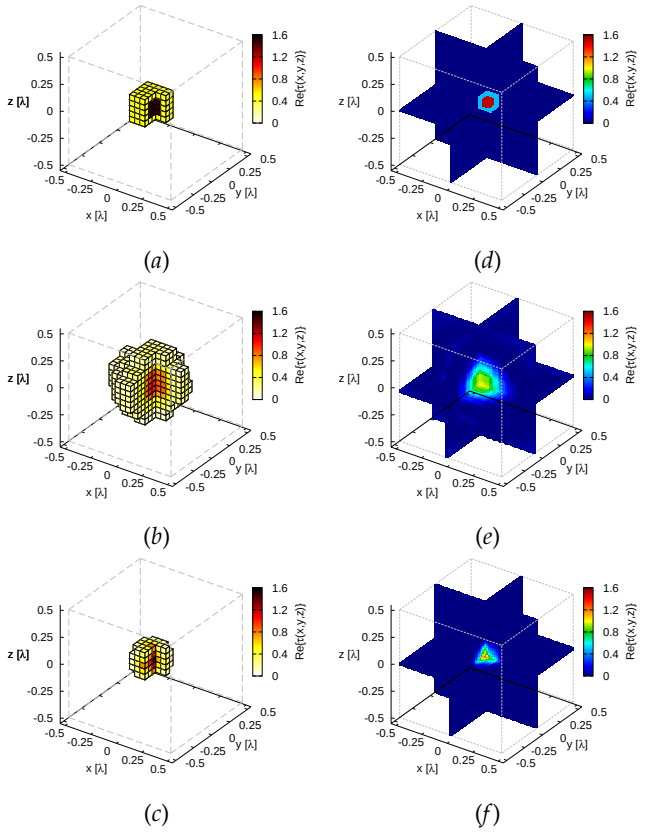

Fig. 13. Three-dimensional representations of the contrast function τ in the investigation domain D_{inv}. Voxels having $\Re\{\tau(x,y,z)\} > 0.1$: (a) true object; (b) bare INLW-3D reconstruction; (c) IMSA-INLW-3D reconstruction with $s = s^{best} = 6$. The region $0 < x < 0.5\lambda \cup -0.5\lambda < y < 0 \cup -0.5\lambda < z < 0.5\lambda$ has been removed to see into the object. Cuts along the three coordinate planes: (d) true object; (e) bare INLW-3D reconstruction; (f) IMSA-INLW-3D reconstruction with $s = s^{best} = 6$. Inhomogeneous object, $SNR = 20\,dB$.

E. Low-contrast objects

In this Section, the reconstructions obtained by means of the IMSA-INLW-3D method in the case of low-contrast targets have been analyzed. A cubic investigation domain D_{inv} of side $L_{D_{inv}} = \lambda$, with barycentre at the origin, has been considered. A set of plane waves originated from $V_\theta = 8$ directions on θ and $V_\phi = 6$ directions on ϕ have been used for illuminating the investigation domain, obtaining a total number of views equal to $V = 38$. The observation domain D_{obs} was composed by $M = 38$ measurement points ($M_\theta = 8$ on θ and $M_\phi = 6$ on ϕ, equally spaced) positioned on a sphere of radius $r_{D_{obs}} = 2\lambda$. The investigation domain has been partitioned into $N_{fwd} = 8000$ cubic cells of side $l_{fwd} = 0.05\lambda$ for solving the forward problem. The number of cubic cells for the IMSA-INLW-3D method has been chosen equal to $N_{IMSA} = 512$, while $N_{BARE} = 1728$ cubic cells of side $l_{BARE} = 0.083\lambda$ have been used for the bare INLW-3D approach. All the control parameters of the IMSA-INLW-3D method have been chosen as in the "Calibration" Section, while $I_{BARE} = 20$ maximum outer Gauss-Newton iterations and $K_{BARE} = 2$ maximum inner Landweber steps have been performed in the bare INLW-3D technique. As can be seen

in Fig. 12(*a*), the investigation domain D_{inv} contains two low-contrast objects, characterized by a contrast function $\tau = 0.2$, with long sides of size $l_{yz} = 0.5\lambda$ and short side of dimension $l_x = 0.15\,\lambda$ spaced by $l_s = 0.35\,\lambda$ along the x axis (i.e., distance between their barycenters). The reconstruction results versus the true dielectric configuration of the investigation domain are presented in Fig. 12, for a noisy case with $SNR = 20\,dB$. With the present target, the bare INLW-3D method [Fig. 12(*b*) and Fig. 12(*e*)] is not able to retrieve a suitable approximation of the dielectric configuration of D_{inv}. In particular, a clear separation between the two objects is missing. On the contrary, the novel IMSA-INLW-3D approach [Fig. 12(*c*) and Fig. 12(*f*)] is capable of correctly reconstructing the two low-contrast targets and the separation between them, even though a slight underestimation of the contrast function value still appears.

F. Inhomogeneous object

The reconstruction of a inhomogeneous target has also been considered. Both the control parameters of the reconstruction methods and the configuration are the same as the previous Section, except for the object, which is an inhomogeneous cube with two layers characterized by different dielectric properties [Fig. 13(*a*)]. An inner cubic region of side $l_{int} = 0.15\lambda$ and centered at the origin has a contrast function equal to $\tau_{int} = 1.5$, while an outer layer with external side $l_{ext} = 0.25\lambda$ is characterized by a contrast function $\tau_{ext} = 0.5$. The results obtained by applying the IMSA-INLW-3D reconstruction method and the bare INLW-3D one with $SNR = 20\,dB$ are reported in Fig. 13. It is evident that both the object size and its dielectric properties are better estimated by the proposed IMSA-INLW-3D technique.

G. Experimental results ("TwoSpheres" target)

The developed strategy has been finally tested by using the experimental data made available from the Institut Fresnel (France). In particular, the "TwoSpheres" target, composed by two spheres with radius 25 mm and relative dielectric permittivity equal to 2.6, has been considered. The detailed description of the measurement setup and of the the target is reported in [48]. In this paper, only the θ-polarized data have been employed for the inversion. In particular, $V = 25$ views has been considered ($V_\theta = 5$ and $V_\phi = 5$ positions of the TX antenna have been selected from the available data by taking one every other position along θ and ϕ). All the available $M = 27$ samples of the measured electric field for every considered view have been used. The first frequency ($f = 3$ GHz) is employed. It is worth noting that the RX antennas are located on a circumference in the $x - y$ plane, consequently only the z-component of the electric field is available. All the other components have been set equal to zero in the scattered field used for the inversion. The investigation domain is a cube of side $L_{D_{inv}} = 1.5\lambda$ centered at the origin. The retrieved three-dimensional dielectric profiles by the IMSA-INLW-3D and INLW-3D are shown in Fig. 14. As it can be observed, a visible improvement of the solution quality is achieved by the IMSA-INLW-3D [i.e., Fig. 14(*b*) vs. Fig. 14(*a*)], showing (*i*) a more accurate estimation of the dielectric permittivity of the targets (the actual contrast function being equal to $\tau = 1.6$), as well as (*ii*) a better resolution. Indeed, differently from its bare counterpart, the IMSA-INLW-3D allows to identify the presence of the two targets, as it is visible by looking at the corresponding two-dimensional cuts for

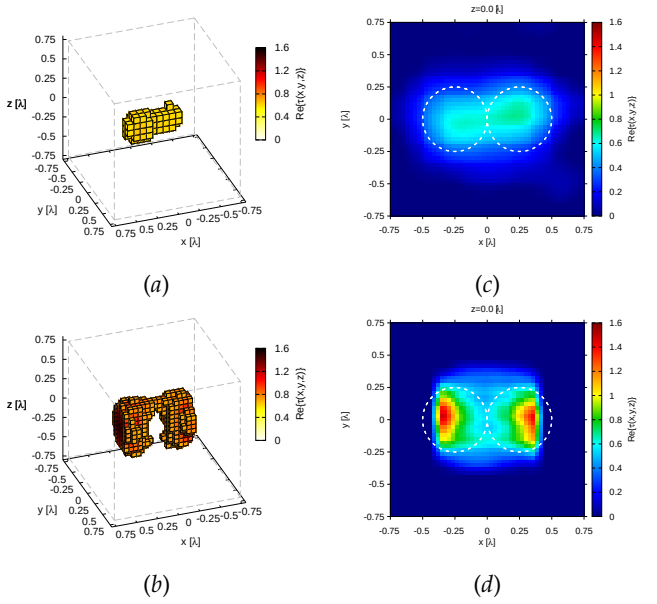

Fig. 14. Three-dimensional representations of the contrast function τ in the investigation domain D_{inv} for the "TwoSpheres" experimental target [48]. Voxels having $\Re\{\tau(x,y,z)\} > 0.6$: (a) bare INLW-3D reconstruction; (b) IMSA-INLW-3D reconstruction with $s = s^{best} = 3$. Two-dimensional cuts for $z = 0$ of the reconstructed distributions of the contrast function τ: (c) bare INLW-3D reconstruction; (d) IMSA-INLW-3D reconstruction.

$z = 0$ reported in Fig. 14(*d*) and 14(*c*), respectively. Finally, concerning the computational times, it is worth observing that a non-negligible reduction of the total execution time is achieved by the IMSA-INLW-3D (i.e., $\frac{\Delta t|_{IMSA-INLW-3D}}{\Delta t|_{INLW-3D}} \approx 0.59$).

4. CONCLUSIONS

In this paper, a novel method for three-dimensional electromagnetic imaging of dielectric targets has been presented and validated. This method is the combination of an inexact-Newton inversion technique with an iterative multiscaling approach. In particular, the main goal was the development of a 3D computationally-effective procedure able to deal with the strong ill-posedness of the underlying inverse scattering problem, faced by exploiting the regularization capabilities of the inexact-Newton method. From one hand, the combined algorithm allows a better usage of the available computational resources. From the other hand, the reduced number of unknowns required by the multiscaling inexact-Newton method allows to reduce the occurrence of local minima, addressing the ill-posedness in a more effective way. The method performance has been assessed throughout several numerical simulations in various operating conditions with different targets and configuration parameters, from canonical configurations to the more challenging cases of inhomogeneous, low contrast and complex dielectric structures. The new approach has been proven to accurately and efficiently reconstruct the electromagnetic properties of objects with different shapes and values of dielectric contrast. Furthermore, the described method appears to be quite robust with respect to the presence of noise on the scattered field data. The representative numerical results also pointed

out the enhanced performance of the combined method versus the "bare" application of the original procedure based on the inexact-Newton technique. Moreover, a preliminary experimental result has been shown, verifying the improved effectiveness of the IMSA-INLW-3D in solving the three-dimensional inverse scattering problem, providing better estimations of the actual contrast function as well as an increased resolution within the identified RoI.

REFERENCES

1. D. Colton and R. Kress, *Inverse acoustic and electromagnetic scattering theory* (Springer New York, 2013).
2. R. Zoughi, *Microwave non-destructive testing and evaluation* (Springer Netherlands, 2000).
3. M. Pastorino, *Microwave imaging* (Wiley, 2010).
4. T. M. Habashy and A. Abubakar, "A general framework for constraint minimization for the inversion of electromagnetic measurements," PIER **46**, 265-312 (2004).
5. P. M. van den Berg and A. Abubakar, "Contrast source inversion method: state of art," PIER **34**, 189-218 (2001).
6. M. Pastorino, "Stochastic optimization methods applied to microwave imaging: a review," IEEE Trans. Antennas Propag. **55**, 538-548 (2007).
7. P. Rocca, M. Benedetti, M. Donelli, D. Franceschini, and A. Massa, "Evolutionary optimization as applied to inverse scattering problems," Inverse Probl. **25**, 1-41 (2009).
8. P. Rocca, G. Oliveri, and A. Massa, "Differential evolution as applied to electromagnetics," IEEE Antennas Propag. Mag. **53**, 38-49 (2011).
9. R. Ferraye, J.-Y. Dauvignac, and C. Pichot, "An inverse scattering method based on contour deformations by means of a level set method using frequency hopping technique," IEEE Trans. Antennas Propag. **51**, 1100-1113 (2003).
10. K. Belkebir and M. Saillard, "Special section: Testing inversion algorithms against experimental data," Inverse Probl. **17**, 1565 (2001).
11. M. Bertero and P. Boccacci, *Introduction to inverse problems in imaging* (IOP Publishing, 1998).
12. O. Bucci and G. Franceschetti, "On the degrees of freedom of scattered fields," IEEE Trans. Antennas Propag. **37**, 918-926 (1989).
13. O. M. Bucci and T. Isernia, "Electromagnetic inverse scattering: retrievable information and measurement strategies," Radio Science **32**, 2123-2137 (1997).
14. T. Isernia, V. Pascazio, and R. Pierri, "On the local minima in a tomographic imaging technique," IEEE Trans. Geosci. Remote Sens. **39**, 1596-1607 (2001).
15. C. Estatico, M. Pastorino, and A. Randazzo, "An inexact-Newton method for short-range microwave imaging within the second-order Born approximation," IEEE Trans. Geosci. Remote Sens. **43**, 2593-2605 (2005).
16. C. Estatico, G. Bozza, A. Massa, M. Pastorino, and A. Randazzo, "A two-step iterative inexact-Newton method for electromagnetic imaging of dielectric structures from real data," Inverse Probl. **21**, S81-S94 (2005).
17. G. Bozza, C. Estatico, M. Pastorino, and A. Randazzo, "An inexact Newton method for microwave reconstruction of strong scatterers," IEEE Antennas Wireless Propag. Letters **5**, 61-64 (2006).
18. G. Bozza and M. Pastorino, "An inexact Newton-based approach to microwave imaging within the contrast source formulation," IEEE Trans. Antennas Propag. **57**, 1122-1132 (2009).
19. A. Massa, P. Rocca, and G. Oliveri, "Compressive sensing in electromagnetics - a review," IEEE Antennas Propag. Mag. **57**, 224-238 (2015).
20. G. Oliveri, P. Rocca, and A. Massa, "A Bayesian-compressive-samplingbased inversion for imaging sparse scatterers," IEEE Trans. Geosci. Remote Sens. **49**, 3993-4006 (2011).
21. L. Poli, G. Oliveri, F. Viani, and A. Massa, "MT-BCS-based microwave imaging approach through minimum-norm current expansion," IEEE Trans. Antennas Propag. **61**, 4722-4732 (2013).
22. L. Poli, G. Oliveri, P. Rocca, and A. Massa, "Bayesian compressive sensing approaches for the reconstruction of two-dimensional sparse scatterers under TE illuminations," IEEE Trans. Geosci. Remote Sens. **51**, 2920-2936 (2013).
23. P. Chiappinelli, L. Crocco, T. Isernia, and V. Pascazio, "Multiresolution techniques in microwave tomography and subsurface sensing," in Proceedings of the IEEE 1999 International Geoscience and Remote Sensing Symposium (IGARSS99), 2516-2518 (1999).
24. O. M. Bucci, L. Crocco, T. Isernia, and V. Pascazio, "An adaptive wavelet-based approach for non-destructive evaluation applications," in Proceedings of the IEEE Antennas and Propagation Society International Symposium, 1756-1759 (2000).
25. O. M. Bucci, L. Crocco, T. Isernia, and V. Pascazio, "Wavelets in nonlinear inverse scattering," in Proceedings of the IEEE 2000 International Geoscience and Remote Sensing Symposium (IGARSS99), 3130-3132 (2000).
26. S. Caorsi, G. L. Gragnani, and M. Pastorino, "A numerical approach to microwave imaging," in Proceedings of the 18th European Microwave Conference, 897-902 (1988).
27. S. Caorsi, M. Donelli, D. Franceschini, and A. Massa, "A new methodology based on an iterative multiscaling for microwave imaging," IEEE Trans. Microw. Theory Techn. **51**, 1162-1173 (2003).
28. G. Oliveri, Y. Zhong, X. Chen, and A. Massa, "Multiresolution subspacebased optimization method for inverse scattering problems," J. Opt. Soc. Am. A **28**, 2057-2069 (2011).
29. G. Franceschini, D. Franceschini, and A. Massa, "Full-vectorial three-dimensional microwave imaging through the iterative multiscaling strategy-A preliminary assessment," IEEE Geosci. Remote Sens. Lett. **2**, 428-432 (2005).
30. G. Oliveri, L. Lizzi, M. Pastorino, and A. Massa, "A nested multiscaling inexact-Newton iterative approach for microwave imaging," IEEE Trans. Antennas Propag. **60**, 971-983 (2012).
31. M. Salucci, G. Oliveri, A. Randazzo, M. Pastorino, and A. Massa, "Electromagnetic subsurface prospecting by a multifocusing inexact Newton method within the second-order Born approximation," J. Opt. Soc. Am. A **31**, 1167-1179 (2014).
32. L. Pan, X. Chen, Y. Zhong, and S. P. Yeo, "Comparison among the variants of subspace-based optimization method for addressing inverse scattering problems: transverse electric case," J. Opt. Soc. Am. A **27**, 2208 (2010).
33. A. Semnani, I. Rekanos, M. Kamyab, and T. Papadopoulos, "Two-dimensional microwave imaging based on hybrid scatterer representation and differential evolution," IEEE Trans. Antennas Propag. **58**, 3289-3298 (2010).
34. A. Litman, D. Lesselier, and F. Santosa, "Reconstruction of a twodimensional binary obstacle by controlled evolution of a level-set," Inverse Probl. **14**, 685 (1998).
35. T. C. Guo, W. W. Guo, S. J. Dwyer III, and R. H. Schneider, *Physics of image formation by microwave scattering* **0767**, 30-39 (1987).
36. S. Caorsi, G. L. Gragnani, and M. Pastorino, "Electromagnetic vision oriented numerical solution to three-dimensional inverse scattering," Radio Sci. **23**, 1094-1106 (1988).
37. M. Ali and M. Moghaddam, "3D nonlinear super-resolution microwave inversion technique using time-domain data," IEEE Trans. Antennas Propag. **58**, 2327-2336 (2010).
38. M. El-Shenawee, O. Dorn, and M. Moscoso, "An adjoint-field technique for shape reconstruction of 3-D penetrable object immersed in lossy medium," IEEE Trans. Antennas Propag. **57**, 520-534 (2009).
39. Z. Q. Zhang and Q. H. Liu, "Three-dimensional nonlinear image reconstruction for microwave biomedical imaging," IEEE Trans. Biomed. Eng. **51**, 544-548 (2004).
40. H. Zhou, T. Takenaka, J. E. Johnson, and T. Tanaka, "A breast imaging model using microwaves and a time domain three dimensional reconstruction method," PIER **93**, 57-70 (2009).
41. J. Johnson, T. Takenaka, K. Ping, S. Honda, and T. Tanaka, "Advances in the 3-D forward-backward time-stepping (FBTS) inverse scattering technique for breast cancer detection," IEEE Trans. Biomed. Eng. **56**, 2232-2243 (2009).
42. J. D. Shea, P. Kosmas, B. D. V. Veen, and S. C. Hagness, "Contrast-

enhanced microwave imaging of breast tumors: a computational study using 3d realistic numerical phantoms," Inverse Probl. **26**, 074009 (2010).
43. J. De Zaeytijd, A. Franchois, C. Eyraud, and J.-M. Geffrin, "Full-wave three-dimensional microwave imaging with a regularized Gauss-Newton method - Theory and experiment," IEEE Trans. Antennas Propag. **55**, 3279-3292 (2007).
44. M. Hajihashemi and M. El-Shenawee, "Level set algorithm for shape reconstruction of non-overlapping three-dimensional penetrable targets," IEEE Trans. Geosci. Remote Sens. **50**, 75-86 (2012).
45. C. Estatico, M. Pastorino, and A. Randazzo, "Microwave imaging of three-dimensional targets by means of an inexact-Newton based inversion algorithm," Int. J. Antennas Propag. **2013**, e407607 (2013).
46. C. A. Balanis, *Advanced engineering electromagnetics* (Wiley, 2012).
47. J. Richmond, "Scattering by a dielectric cylinder of arbitrary cross section shape," IEEE Trans. Antennas Propag. **13**, 334-341 (1965).
48. J M. Geffrin and P. Sabouroux, "Continuing with the Fresnel database: experimental setup and improvements in 3D scattering measurements," Inverse Probl. **25**, 024001 (2009).